AIAA SciTech
5-9 January 2015, Kissimmee, Florida
53rd AIAA Aerospace Sciences Meeting

Normal Incidence Acoustic Transmission Loss of Perforated Plates with Bias Flow

Vincent Phong[1] and Dimitri Papamoschou[2]
University of California, Irvine, CA 92697, USA

A study has been conducted on the transmission of sound at normal incidence through perforated plates with bias flow. A theoretical model is proposed which characterizes the acoustic response of the plate through the insertion loss. The proposed model is based on inviscid, one-dimensional wave propagation and mean flow through a single contraction/expansion chamber and includes hole interaction effects. Entropy fluctuations are used to model losses in acoustic energy that occur in the mixing region downstream of the perforations. Experimental measurements of insertion loss are conducted in a specially designed facility and are used to assess the validity of the model over a range of plate thickness, porosity, and hole size. Further, the model is compared to past theoretical treatments. The experimental results indicate an increase in insertion loss with increasing frequency, followed by saturation and decline as resonant conditions are established in the perforations. There is an increase in insertion loss as the Mach number through the perforation increases from 0 to about 0.25, and the resonance frequency decreases with increasing Mach number. The proposed model captures these trends and its predictions are superior to those of past models. Experimental measurements of insertion loss at higher hole Mach numbers are challenging as the turbulent fluctuations in the mixing region can overwhelm the acoustic signal transmitted through the perforation.

Nomenclature

A	=	area
a	=	perforation radium
C_c	=	contraction coefficient
C_D	=	discharge coefficient
c	=	wave propagation speed
d	=	perforation diameter
f	=	frequency
I	=	incident pressure amplitude or acoustic intensity
IL	=	intensity level
k	=	acoustic wave number
K_R	=	Rayleigh conductivity
L_T	=	transmission loss
L_I	=	insertion loss
l	=	plate thickness
l'	=	end correction
M	=	Mach number
$\dot{m}$	=	mass flow rate

[1] Graduate Student Researcher, Department of Mechanical and Aerospace Engineering, vphong@uci.edu, AIAA Student Member.
[2] Professor, Department of Mechanical and Aerospace Engineering, dpapamos@uci.edu, AIAA Fellow.

P = hole spacing between perforations
p = static pressure
PL = power level
Re = Reynolds number
R_{m1m2} = cross correlation of microphones signals
SPL = sound pressure level
SNR = signal-to-noise ratio
St = Strouhal number
St_a = acoustic Strouhal number
T = transmitted pressure amplitude
T_c = transmission coefficient
u = velocity
Z = perforation impedance
z = normalized perforation impedance $=Z/\rho c$
β = porosity of perforated plate
γ = ratio of specific heats c_p/c_v
γ^2 = magnitude of coherence squared
ΔL_I = insertion loss level difference between model and experiment
δ = entropy fluctuation
λ = acoustic wavelength
ν = kinematic viscosity
ρ = density
ψ = Fok's function
ω = angular frequency
$( )'$ = acoustic perturbation

Subscripts

0 = baseline
1 = region upstream of contraction
2 = region inside the contraction, or in the perforation
3 = region downstream of contraction
e = effective
exp = experimental
m = mixing region
ref = reference value
vc = *vena contracta*

I. Introduction

Perforated plates are employed in various noise control applications, such as mufflers in automotive exhaust systems, liners in turbofan engines, and pneumatic bleed valves. Mean fluid flow is typically present in these applications, and is directed either at tangential incidence, normal incidence, or a combination of both with respect to the plane of the perforated plate. Fluid flow that is directed normal to the perforated plate, such that the flow is forced through the perforations, is referred to as bias flow. In the linear regime of acoustic excitations, a perforated plate behaves as a low-pass acoustic filter when no mean flow is present. The characteristics of attenuation are determined by the perforated plate's physical parameters[1], such as the porosity, β, plate thickness, l, and hole diameter, d. The addition of bias flow through the perforations introduces potential benefits in the absorptive properties of the plate.

Losses in acoustic energy occur at area discontinuities, where the energy of an acoustic wave is transferred to the kinetic energy of vortical motions in the shear layer. The kinetic energy of the vortical motions is ultimately

dissipated as heat. This implies a non-isentropic process downstream of the perforated plate, where changes in entropy must be factored into the propagation of the acoustic field. Mungur and Gladwell[2] linearized the energy equation in terms of entropy, and obtained an expression relating entropy fluctuations to acoustic pressure fluctuations. Ronneberger[3], Alfredson and Davies[4], Davies[5] and Cummings[6] applied this concept to a duct containing a sudden expansion. Ronneberger and Cummings provided experimental measurements of reflection coefficient that were in good agreement for flow Mach number < 0.6. Their results[3,6] indicated a monotonic increase in losses with increasing duct Mach number. More recently, Hofmans *et al.*[7] and Durrieu *et al.*[8] developed a quasi-steady model of the acoustic response of a circular diaphragm and a perforated plate, respectively, in a duct with bias flow, using entropy fluctuations to model the dissipation of acoustic energy. For low frequency excitations, their results indicated increasing transmission loss with increasing bias flow speed.

Numerous investigations have been dedicated to the study of the transmission characteristics of perforated plates with bias flow; however, only few of these studies provided theoretical analyses that addressed the effect of flow on the acoustic interaction between the perforations. A recent study[9] indicated that applications exist outside of the parameter space (porosity, Mach number, and acoustic frequency) where previous theoretical models were validated. The present investigation consists of both experiments and theoretical modeling of the transmission characteristics of perforated plates subject to bias flow. The proposed model is based on the one-dimensional analysis conducted by Durrieu *et al.*[8] with additional consideration to bias flow effects on the acoustic energy dissipation and interaction between perforations. The experiments in this study utilize a broadband noise source, allowing the transmission characteristics of perforates to be obtained over a wide spectrum of frequencies in a single experiment run. Insertion loss measurements are obtained for perforated plates over a comprehensive range of porosity, hole diameter, plate thickness, and bias flow speeds. The proposed model will be validated by comparison with experimental results and previous models.

II. Theoretical Modeling

A. Previous Models

Howe[10] proposed an analytical model for the Rayleigh conductivity of a circular aperture in an infinitely thin plate subject to low Mach number bias flow. He assumed that a circular, cylindrical vortex sheet is shed downstream of the aperture, at a strength determined by the condition that u' and p' remain finite at the rim of the aperture. The theory was extended to a perforated screen with the assumption that the perforations were sufficiently separated such that the flow details of neighboring apertures do not influence each other. The results indicated significant attenuation at low Strouhal numbers based on orifice radius and orifice mean flow velocity. The level of attenuation decreased with increasing Strouhal number. The model is applicable for low Mach number flow, low porosity, and acoustic wavelengths that significantly exceed the perforation dimensions. Howe characterizes the performance of the perforated plate using the Rayleigh conductivity, which is an equivalent expression for the acoustic admittance

$$K_R = 2a\left\{1+\frac{\frac{\pi}{2}I_1(St_a)e^{-St_a}-iK_1(St_a)\sinh(St_a)}{St_a\left[\frac{\pi}{2}I_1(St_a)e^{-St_a}+iK_1(St_a)\cosh(St_a)\right]}\right\} \tag{1}$$

Here, $St_a = \omega a/u_2$ is the Strouhal number based on the bias flow velocity through the aperture, u_2, and the aperture radius, a, and I_1 and K_1 are the modified Bessel functions of the first and second kind, respectively. The real and imaginary components of Eq. 1 are expressed in normalized form as $\gamma_R=\mathrm{Re}\{K_R/(2a)\}$ and $\delta_R=\mathrm{Im}\{K_R/(2a)\}$, respectively. Howe defined the transmission coefficient as

$$T_c = \frac{(4\beta/\pi M_2)(\gamma_R - i\delta_R)}{\left|St_a + (i4\beta/\pi M_2)(\gamma_R - i\delta_R)\right|^2} \tag{2}$$

where the $M_2 = u_2/c$ is the Mach number of the flow in the perforations, and β is the porosity of the plate. The accuracy of this model was corroborated experimentally by Hughes and Dowling[11] and by Eldredge and Dowling[12]. Collectively, these authors verified Howe's model for $2.18\times10^{-4} \le d/\lambda \le 0.016$, $0.02 \le \beta \le 0.11$, and $0 \le M_2 \le 0.09$. The transmission loss, or level difference between the incident and transmitted sound power, is determined from Eq. 2

$$L_T = -20\log_{10}(T_c) \tag{3}$$

Jing and Sun[13] investigated the effect of thickness on the acoustic impedance of perforated plates with bias flow. The authors recast Howe's analytical expression[10] for the Rayleigh conductivity in terms of the normalized acoustic impedance of the perforated plate. An additional reactance term was included to account for plate thickness, resulting in the following expression

$$z = \left(\frac{\pi ka}{2\beta}\right)\left(\frac{\delta_R}{\gamma_R^2+\delta_R^2} - i\frac{\gamma_R}{\gamma_R^2+\delta_R^2}\right) + i\frac{kl}{\beta} \tag{4}$$

The acoustic impedance was measured experimentally using an impedance tube setup, and their model[13] was validated over a range of for $0.0129 \le \beta \le 0.0254$, $0.0027 \le d/\lambda \le 0.011$, and $0 \le M_2 \le 0.08$. Jing and Sun's experimental measurements and model predicted an increase in absorption with increasing plate thickness.

Betts[14] modified Crandall's impedance model[15] to account for high Mach number bias flow. He obtained an expression for the normalized perforation impedance

$$z = \frac{16\nu l}{c\beta C_D d^2} + 2.82\frac{\sqrt{\omega\nu}}{c\beta C_D}\frac{l}{d} + \frac{\rho}{\rho_2}\frac{(1-\beta^2)}{2c(\beta C_D)^2}\left[2u_b + 1.2u_{rms}\right] + i\left(\frac{\omega l}{c\beta C_D} + 2.82\frac{\sqrt{\omega\nu}}{c\beta C_D}\frac{l}{d} + \frac{8d}{3\pi\psi(\beta)}\right) \tag{5}$$

ρ, c, ν, u_b and u_{rms} are the density, propagation speed, kinematic viscosity of air, bias flow and root mean square (rms) velocity, respectively, upstream of the plate. $C_D = 0.76$ is the discharge coefficient and ψ includes the effect of interaction between perforations (to be introduced in Section II.B). Betts estimated the rms velocity experimentally, using the plane wave relation between the acoustic velocity and the sound pressure level

$$|u'| = \frac{p_{ref}\,10^{SPL/20}\sqrt{2}}{\rho c} \tag{6}$$

where $p_{ref} = 2\times10^{-5}$ Pa is the reference pressure. Experimental validation was provided for $0.0007 \le d/\lambda \le 0.0129$, $0.059 < \beta < 0.165$, and $0.00221 \le M_2 \le 0.357$.

The impedance models presented by Jing and Sun[13] and Betts[14] can be rewritten as an expression for transmission loss by examining the classic problem of acoustic wave transmission between two semi-infinite fluid media: one defined by the characteristic impedance of the air upstream of the perforated plate, and the other by the perforation impedance. The resultant expression is

$$L_T = -10\log_{10}\left(1 - \left|\frac{Z-\rho c}{Z-\rho c}\right|^2\right) \tag{7}$$

where ρc is the characteristic impedance upstream of the plate, and $Z = z\rho_2 c_2$ is the perforation impedance. Equations 7 and 3 use transmission loss to describe the acoustic performance of the perforated plate. It was previously noted that the transmission loss is the level difference between the acoustic power of the incident and transmitted wave. This requires acoustic measurements both upstream and downstream of the perforated plate, which can be difficult to obtain accurately for in-duct acoustic measurements. In this case, the insertion loss, L_I, is a more convenient performance criterion, and is defined as the difference in sound power level at the same location downstream of the perforated plate, with and without the perforation installed.

Table 1 lists the maximum values of experimental parameters at which previous investigations[10,13,14] validated their respective models. Howe[10] and Jing and Sun[13] focused on low porosity plates such that the mean flow and acoustic interactions between the perforations can be ignored. Both analyses assumed negligible changes in the mean flow density, and their respective models were validated only for small bias flow Mach number. Mass end correction and *vena contracta* effect were not included in these investigations[10,13]. Betts accounted for end effects higher bias flow Mach numbers, and higher porosity, however, the range of validation is still restricted to porosity values less than those employed on bleed valve silencers[9]. *Vena contracta* was included in his analysis through the discharge coefficient, which was assumed constant. The proposed model presented in this study (to be presented in Section II.B) aims to rectify the shortcomings of previous models[10,13,14]. End effects and interactions between the perforations are considered in this work. An estimate of the *vena contracta* location was used to determine the effect of bias flow on the end correction of a perforated plate. The *vena contracta* was not assumed constant;

empirical data was used to determine the discharge coefficient as a function of bias flow speed, porosity, thickness, hole diameter, and the spacing between perforations..

Table 1 Summary of previous insertion loss models and validated parametric space.

Investigator(s)	Maximum β	Maximum M_2	Maximum d/λ	*Vena contracta*	Mass end correction	Hole interaction effect
Howe (1979)	0.11	0.09	0.016	--	--	--
Jing & Sun (2000)	0.03	0.08	0.011	--	--	--
Betts (2000)	0.17	0.36	0.013	constant	$8d/3\pi$	$\psi(\beta)$

B. Proposed Model

In the present study, the insertion loss of perforated plates with bias flow is based on the work of Durrieu *et al.*[8] and Hofmans *et al.*[7]. The perforated plate is modeled as a duct containing a single contraction chamber with mean flow along the duct axis (Fig. 1a). The subscripts 1, 2, j, m, and 3 are used as reference to regions upstream of the contraction, within contraction, the *vena contracta* location, the mixing region downstream of the contraction, and the fully mixed region, respectively. The contraction is a discontinuous change in area at $x = 0$, and the ratio of contracted area to upstream area is defined by $\beta = A_2/A_1$. The contraction expands discontinuously at $x = l$ to the original duct area, $A_3 = A_1$. The Reynolds number ($u_2 d/\nu$) in the contraction is assumed to be sufficiently large so that viscosity has the sole effect of flow separation at the upstream corner of the contraction, as illustrated by the blue dashed lines in Fig 1a. A jet forms downstream of the contraction plane (x=0), and contracts to a minimum area A_{vc} at the *vena contracta* ($x = l_{vc}$). Here, the density, pressure and Mach number M_j are approximately uniform. Irreversible losses occur in the mixing region downstream of the *vena contracta*; the losses are represented in this study through fluctuations in entropy. After some distance l_m downstream from the expansion, the acoustic and mean flow properties are approximated as one-dimensional in region 3.

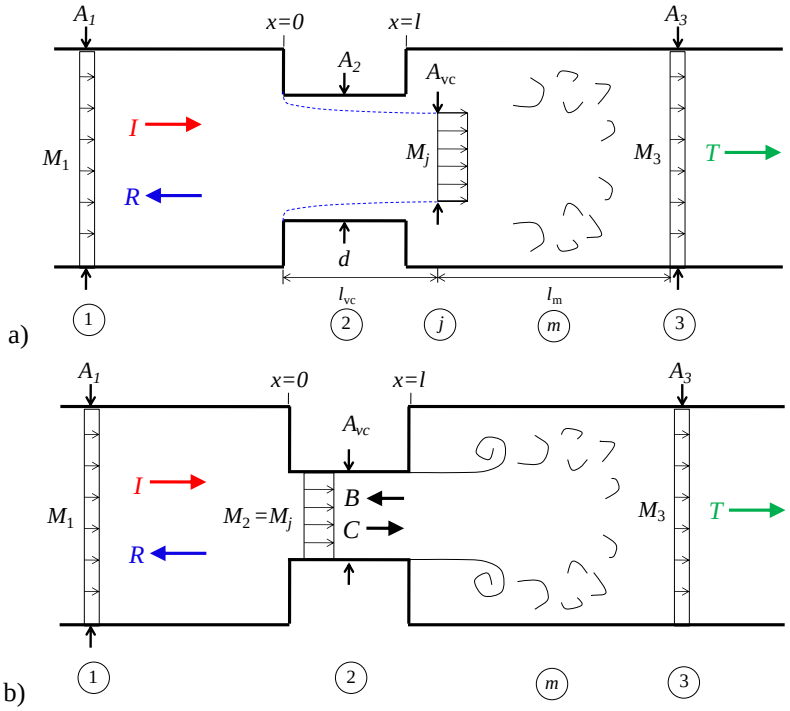

Fig. 1 Contraction chamber used for modeling perforated plate acoustics a) with contraction area corresponding to perforation diameter and b) with contraction area equal to the *vena contracta* area.

In the following analysis, the mean flow in region 2 is approximated as one-dimensional and parallel to the duct axis. The change in mean flow speed is discontinuous at $x = 0$, and the separation of the jet and its profile is

modeled as a contraction of constant area, equal to the *vena contracta* area (Fig. 1b). The jet Mach number $M_2 = M_j$ is subsonic, and the acoustic wavelength is assumed to be much larger than the contraction diameter. This allows the approximation of one-dimensional acoustic wave propagation in regions 1, 2, and 3 of the duct.

The acceleration of mean flow between regions 1 and 2 is assumed inviscid and isentopic. The following integral forms for conservation of mass and energy apply, along with the isentropic relation:

$$\rho_1 u_1 = \rho_2 u_2 \beta C_c \tag{8}$$

$$\frac{\gamma}{\gamma - 1}\frac{p_1}{\rho_1} + \frac{u_1^2}{2} = \frac{\gamma}{\gamma - 1}\frac{p_2}{\rho_2} + \frac{u_2^2}{2} \tag{9}$$

$$\frac{p_1}{\rho_1^\gamma} = \frac{p_2}{\rho_2^\gamma} \tag{10}$$

Equation 8 implies that the *vena contracta* area $A_{vc} = A_2 = A_1 \beta C_c$. Downstream of the duct expansion, the conservation equations are applied to the control volume illustrated in Fig. 2

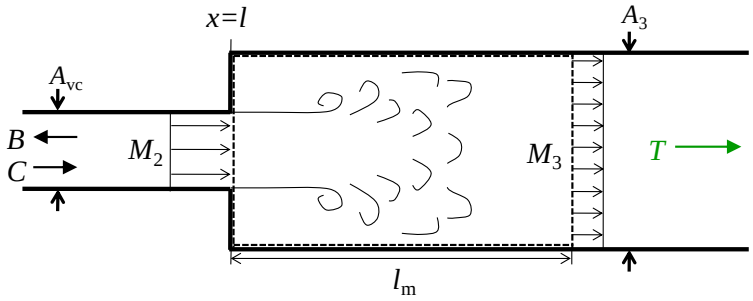

Fig. 2 Control volume containing the mixing region downstream of the expansion.

The control volume (dashed black line) is defined such that the left surface is located at $x = l$. The top and bottom surfaces are coincident with the walls of the duct, and the right surface is located at length l_m that is sufficiently downstream of the expansion so that the jet is completely mixed and the flow properties are uniform along this surface. Mass conservation between the left ($x = l$) and right ($x = l + l_m$) surfaces of the control volume requires that

$$\rho_2 u_2 \beta C_c = \rho_3 u_3 \tag{11}$$

Assuming that the flow expands adiabatically

$$\frac{\gamma}{\gamma - 1}\frac{p_2}{\rho_2} + \frac{u_2^2}{2} = \frac{\gamma}{\gamma - 1}\frac{p_3}{\rho_3} + \frac{u_3^2}{2} \tag{12}$$

Neglecting friction along the walls of the duct, the momentum conservation between the left and right surfaces of the control volume yields

$$p_2 + \rho_2 u_2^2 \beta C_c = p_3 + \rho_3 u_3^2 \tag{13}$$

The contraction coefficient C_c in Eqs. 8, 11 and 13 can be determined from the discharge coefficient $C_c = C_D/0.98$. The discharge coefficient C_D is determined based on the empirical correlation formula provided by Smith and Van Winkle[16] for perforated plates

$$C_D = K\left(\frac{d}{P}\right)^{0.10} \tag{14}$$

where K is specified by the Reynolds number in the contraction, $\mathrm{Re}_2 = u_2 d/\nu$, and l/d, using Fig. 9 from Ref. 16. The distance between perforations, P, is determined based on the pattern of the perforation grating. For a rectilinear pattern, P is defined as[17]

$$P = 0.89\frac{d}{\sqrt{\beta}} \tag{15}$$

and for a triangular pattern

$$P = 0.9498\frac{d}{\sqrt{\beta}} \tag{16}$$

Equations 8-13 define the mean flow properties throughout the entire domain. Assuming time harmonic disturbances of the exponential form $e^{i\omega t}$, where $\omega=2\pi f$ is the angular frequency, the acoustic pressure throughout the domain in Fig. 1b can be expressed as

$$\begin{aligned} p'(x,t) &= I\,e^{i\left(\omega t-\frac{kx}{1+M_1}\right)} + R\,e^{i\left(\omega t-\frac{kx}{1-M_1}\right)} && ,\ x<0 \\ p'(x,t) &= B\,e^{i\left(\omega t-\frac{kx}{1+M_2}\right)} + C\,e^{i\left(\omega t-\frac{kx}{1-M_2}\right)} && ,\ 0\le x\le l \\ p'(x,t) &= T\,e^{i\left(\omega t-\frac{kx}{1+M_3}\right)} && ,\ x>l \end{aligned} \tag{17}$$

For one-dimensional, isentropic wave propagation, the velocity and density fluctuations are related to pressure fluctuations as the following

$$u' = \frac{\pm p'}{\rho c} \tag{18}$$

$$\rho' = \frac{p'}{c^2} \tag{19}$$

Equation 19 is applicable where the mean flow is isentropic. Irreversible flow losses occur due to mixing and viscous dissipation as the flow develops downstream of the contraction (Fig. 2). The losses associated with the flow in the mixing region produce fluctuations in entropy that propagate downstream at the mean flow velocity in region 3. The use of entropy fluctuations to describe the dissipation in acoustic energy has been used by previous researchers[2-8] with experimental validation[3,4,6,7]. The method of characterizing dissipation through entropy fluctuations can readily be integrated into the perturbed energy equation, using principles from thermodynamics. The acoustic density fluctuation in region 3 can be expanded in terms of pressure and entropy fluctuations[2]

$$\rho_3' = \frac{p_3'}{c_3^2} - \frac{\bar{\rho}_3\bar{T}_3(\gamma-1)s_3'}{c_3^2} \tag{20}$$

where the overbar indicates the quantity associated with the mean state of the fluid. The second term on the right hand side of Eq. 20 indicates a perturbation from the isentropic relation defined in Eq. 19. Equation 20 can be rewritten in the form

$$\rho_3' = \frac{p_3' + \delta}{c_3^2} \tag{21}$$

δ is finite only in region 3 because the entropy fluctuations produced in region m are convected downstream by the mean flow. Since the entropy fluctuations propagate at speeds corresponding to the mean velocity in region 3, these fluctuations are not directly involved in the propagation of true sound, and therefore do not contribute to the generation of sound power in the duct. The entropy fluctuations are equal to zero in both regions 1 and 2, because the flow processes there are assumed isentropic.

Phong and Papamoschou[1] showed that the end effects associated with the acoustic radiation from open ended tubes are an essential component in modeling the transmission behavior of perforated plates without bias flow. The

end correction included interactions between the perforations in the form of a correction to the physical thickness of the plate (Fig. 3a)

$$l' = \frac{8d}{3\pi\psi(\beta)} \tag{22}$$

where $\psi(\beta)$ is a function derived by Fok that describes the acoustic interactions between the perforations[18]. Equation 22 was found to be accurate in describing the transmission behavior of a perforated plate without bias flow[1], and consequently must be modified to include the effect of mean flow. Fok's function[18] was derived based on potential theory, and therefore it is assumed that Eq. 22 is applicable only where the mean flow is irrotational. Melling[19] proposed a qualitative explanation of the effect of bias flow on the end correction associated with perforated plates. The author stated that "up to the *vena contracta* the flow is laminar and becomes turbulent beyond it… the mass reactance due to the attached mass is presumed to exist and beyond this point is destroyed." Therefore the modification to the attached mass is determined as a function of the *vena contracta* location of the jet. Figure 3b schematically illustrates this effect for a single perforation.

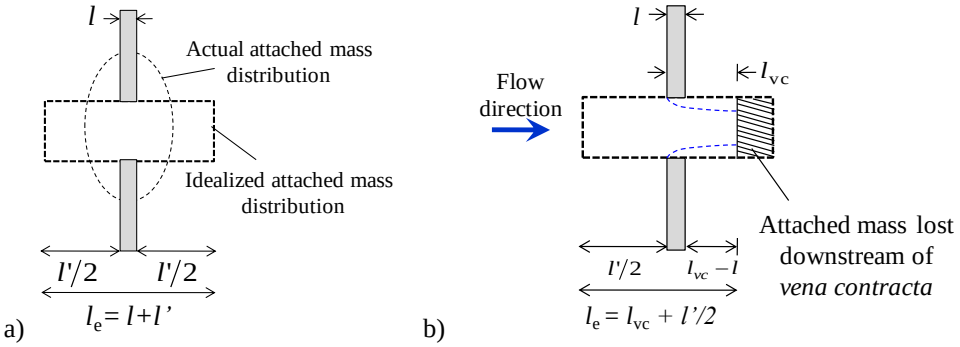

Fig. 3 End correction associated with a single perforation a) without bias flow; b) with modification that account for bias flow.

The *vena contracta* length, l_{vc}, is defined as the distance between the upstream surface of the plate and the *vena contracta* location. The *vena contracta* location is approximated using the jet profile determined numerically by Rouse and Abul-Fetouh[20]. Based on their data, the jet diameter contraction ratio *d/D* is within 1% of the fully contracted value at *x/a* =1.4, and therefore it is assumed in this work that the *vena contracta* is located at l_{vc}=1.4*a*. Observing Figs. 3a and 3b, three cases are defined which scale the end correction with respect to l_{vc}:

$$\begin{aligned} l_e &= l + l' \quad ; \quad l_{vc} > l'/2 \\ l_e &= l'/2 + l_{vc} \quad ; \quad l < l_{vc} < l'/2 \\ l_e &= l + l'/2 \quad ; \quad l_{vc} < l \end{aligned} \tag{23}$$

where l' corresponds to the end correction length defined in Eq. 22. Observing Eq. 23, the first condition implies that the end correction length for perforations with bias flow cannot be larger than the end correction without bias flow. The second condition follows Melling's assumption that the static end correction length on the downstream side of the plate is limited by the *vena contracta* length. The third condition implies that although the *vena contracta* location resides within the contraction, significant mixing does not occur until the flow leaves the perforations, and therefore the mean flow is approximately potential inside the perforation.

Applying acoustic perturbations to p, ρ and u, and making the appropriate linearization results in the following set of equations

$$\frac{\beta C_c}{c_2}\left[(1+M_2)Be^{-ik_2^+ l_e} - (1-M_2)Ce^{ik_2^- l_e}\right] = \frac{1}{c_3}\left[(1+M_3)Te^{-ik_3^+(l_e+l_m)} + M_3\delta e^{-ik_\sigma^+(l_e+l_m)}\right] \tag{24}$$

$$\frac{1}{c_1}\left[(1+M_1)I - (1-M_1)R\right] = \frac{C_c\beta}{c_2}\left[(1+M_2)B - (1-M_2)C\right] \tag{25}$$

$$\left[\beta C_c\left(M_2^2+2M_2\right)+1\right]Be^{-ik_2^+ l_e}+\left[\beta C_c\left(M_2^2-2M_2+1\right)\right]Ce^{ik_2^- l_e}=\left(1+M_3\right)^2 Te^{-ik_3^+(l_e+l_m)}+M_3^2\delta e^{-ik_\sigma^+(l_e+l_m)} \quad (26)$$

$$\frac{1}{\bar{\rho}_2}\left[\left(1+M_2\right)Be^{-ik_2^+ l_e}+\left(1-M_2\right)Ce^{ik_2^- l_e}\right]=\frac{1}{\bar{\rho}_3}\left[\left(1+M_3\right)Te^{-ik_3^+(l_e+l_m)}-\frac{\delta}{\gamma-1}e^{-ik_\sigma^+(l_e+l_m)}\right] \quad (27)$$

$$\frac{1}{\bar{\rho}_1}\left[\left(1+M_1\right)I+\left(1-M_1\right)R\right]=\frac{1}{\bar{\rho}_2}\left[\left(1+M_2\right)B+\left(1-M_2\right)C\right] \quad (28)$$

Equations 24 and 25 are the continuity equations applied from regions 2 to 3, and 1 to 2, respectively; Eq. 26 is the momentum conservation between the jet and fully mixed flow in region 3; and Eqs. 27 and 28 are the energy conservation equations from regions 2 to 3, and 1 to 2, respectively. Equations 24-28 are a linear system of equations which can be written in the form of a scattering matrix

$$\begin{pmatrix} 0 & K_5 & K_6 & -K_3 & -K_4 \\ K_2 & -K_7 & -K_8 & 0 & 0 \\ 0 & K_9 & K_{10} & -K_{11} & -K_{12} \\ 0 & -K_{17} & -K_{18} & K_{15} & K_{16} \\ K_{14} & -K_{19} & -K_{20} & 0 & 0 \end{pmatrix}\begin{pmatrix} R \\ B \\ C \\ T \\ \delta \end{pmatrix}=\begin{pmatrix} 0 \\ -K_1 \\ 0 \\ 0 \\ -K_{13} \end{pmatrix}I \quad (29)$$

$$K_1=\frac{1+M_1}{c_1} \qquad K_6=-\beta C_c\frac{1-M_2}{c_2}e^{ik_2^- l_{e,b}} \qquad K_{11}=\left(1+M_3\right)^2 e^{-ik_3^+(l_{e,b}+l_m)} \qquad K_{16}=\frac{-1}{\bar{\rho}_3(\gamma-1)}e^{-ik_\delta(l+l_m)}$$

$$K_2=-\frac{1-M_1}{c_1} \qquad K_7=\beta C_c\frac{1+M_2}{c_2} \qquad K_{12}=M_3^2 e^{-ik_\delta(l_{e,b}+l_m)} \qquad K_{17}=\frac{1+M_2}{\bar{\rho}_2}e^{-ik_2^+ l_{e,b}}$$

$$K_3=\frac{1+M_3}{c_3}e^{-ik_3^+(l+l_m)} \qquad K_8=-\beta C_c\frac{1-M_2}{c_2} \qquad K_{13}=\frac{1+M_1}{\bar{\rho}_1} \qquad K_{18}=\frac{1-M_2}{\bar{\rho}_2}e^{ik_2^- l_{e,b}}$$

$$K_4=\frac{M_3}{c_3}e^{-ik_\delta(l+l_m)} \qquad K_9=\beta C_c\left[M_2^2+2M_2\right]e^{-ik_2^+ l_{e,b}} \qquad K_{14}=\frac{1-M_1}{\bar{\rho}_1} \qquad K_{19}=\frac{1+M_2}{\bar{\rho}_2}$$

$$K_5=\beta C_c\frac{1+M_2}{c_2}e^{-ik_2^+ l_{e,b}} \qquad K_{10}=\beta C_c\left[M_2^2-2M_2\right]e^{ik_2^- l_{e,b}} \qquad K_{15}=\frac{\left(1+M_3\right)}{\bar{\rho}_3}e^{-ik_3^+(l_{e,b}+l_m)} \qquad K_{20}=\frac{1-M_2}{\bar{\rho}_2}$$

The system of equations is solved using Matlab's inbuilt reduced row echelon function. The acoustic energy flux of a plane wave propagating along the same direction as a medium in motion is expressed as[21]

$$I=\frac{1}{\bar{\rho}c}\left[\left(1+M\right)^2\left\langle p'^2\right\rangle\right] \quad (30)$$

where the angle brackets denote time averaging. The acoustic power is determined by multiplying Eq. 30 by the appropriate duct area. Since $A_1 = A_3$, the transmission loss is therefore determined from Eq. 30

$$L_T=10\log_{10}\left(\frac{\bar{\rho}_3 c_3}{\bar{\rho}_1 c_1}\frac{\left(1+M_1\right)^2}{\left(1+M_3\right)^2}\frac{\left|I\right|^2}{\left|T\right|^2}\right) \quad (31)$$

where T is known from the solution of Eq. 29. In the absence of an area contraction and viscosity, the incident wave in region 1 propagates downstream to region 3 without any loss in power, and therefore Equation 31 is also a valid expression for the insertion loss ($L_T = L_I$).

III. Experiment Setup

The arrangement by which acoustic experiments were tested is illustrated in Fig. 4. The setup is similar to an impedance tube, with modifications to include bias flow. The facility was divided into three sections, all connected by pipe flanges. The internal diameter of the duct is 26.35-cm. Internal reflections from the duct walls were minimized by installing 3.8-cm duct liner in all sections, resulting in an effective internal diameter of 18.73 after installation of the liner. In the flow conditioning section, compressed air was supplied radially through four injection ports. 0.32-cm cell size honeycomb followed by a series of screens were employed to minimize turbulence fluctuations of flow in the duct. A relief valve was installed upstream of the screens with burst pressure of 34.5 kPa. Downstream of the conditioning section, an impinging jets setup[22] was used to simulate a broadband monopole-type noise source. The impinging jets were supplied at a pressure 517 kPa by four 1.6-mm diameter tubes, resulting in a net mass flow rate $\dot{m} = 9.81\times10^{-4}$ kg·m^{-3}. At the end of the source section, a bell-shaped convergent section 20.7-cm in length was constructed using open cell, insulation foam sealant. The area contraction ratio of this section is 16.8, resulting in a contraction diameter of 4.57-cm immediately upstream of the sample mounting plate. The convergent section permitted a broad variation of subsonic bias flow speeds and ensured uniform axial flow at the sample mounting plate. The sample mounting plate had a 4.57-cm diameter hole bored in its center that allowed airflow through from the convergent section. The perforated plates were mounted on the downstream surface of the sample mounting plate over the center-bored hole. A 3.2-mm condenser microphone (Brüel & Kjaer, Model 4138) with a frequency response of 140 kHz was mounted on a traversable arm. The microphone orientation was parallel to the duct axis. To prevent reflections from the end of the measurement section, a sound absorbing cone was installed.

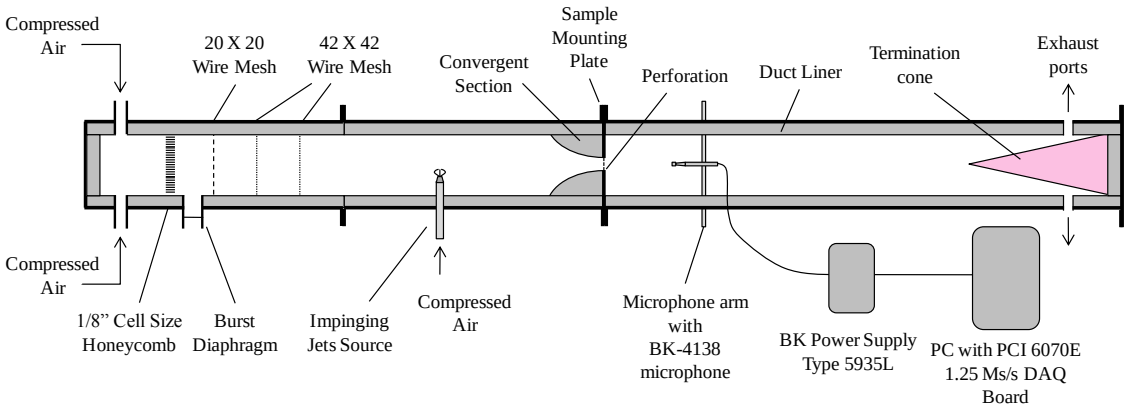

Fig. 4 Schematic of experimental setup.

The sound power in the duct was acquired by spatially averaging the sound intensity downstream of the perforated plate. The local intensity was computed based on the sound pressure level (SPL), which was measured at 19 radial locations, each separated by 6.4-mm, at a fixed axial location from the sample mount. A nosecone (G.R.A.S. Model RA0173) was attached to the microphone to minimize flow induced noise. The microphone was connected to a dual channel power supply/conditioning amplifier (Brüel & Kjaer Type 5935L). The output of the signal was sampled at 250 kS/s by a multifunction data acquisition board (National Instruments PCI-6070E) installed in a Dell Optiplex 380 personal computer with an Intel Core 2 Duo processor. National Instruments LabView software was used to acquire the microphone signal. The resultant signal was conditioned with a high-pass filter set at 350 Hz. The narrowband spectra were computed using a 4096-point (Δf = 61 Hz) Fast Fourier Transform and were corrected for microphone frequency response, free-field response, and atmospheric absorption. The experimental insertion loss (L_I) was measured based on the difference in the sound power level spectrum with and without (baseline case) the perforated plate attached to the sample mounting plate. Figure 5 details the setup for measuring the acoustic power downstream of the perforated plate. Multiple spatial measurements were obtained by traversing the microphone along the axis of the arm (Fig. 5a). Figure 5b details the measurement plane and locations at which the acoustic signals were acquired to determine the sound power.

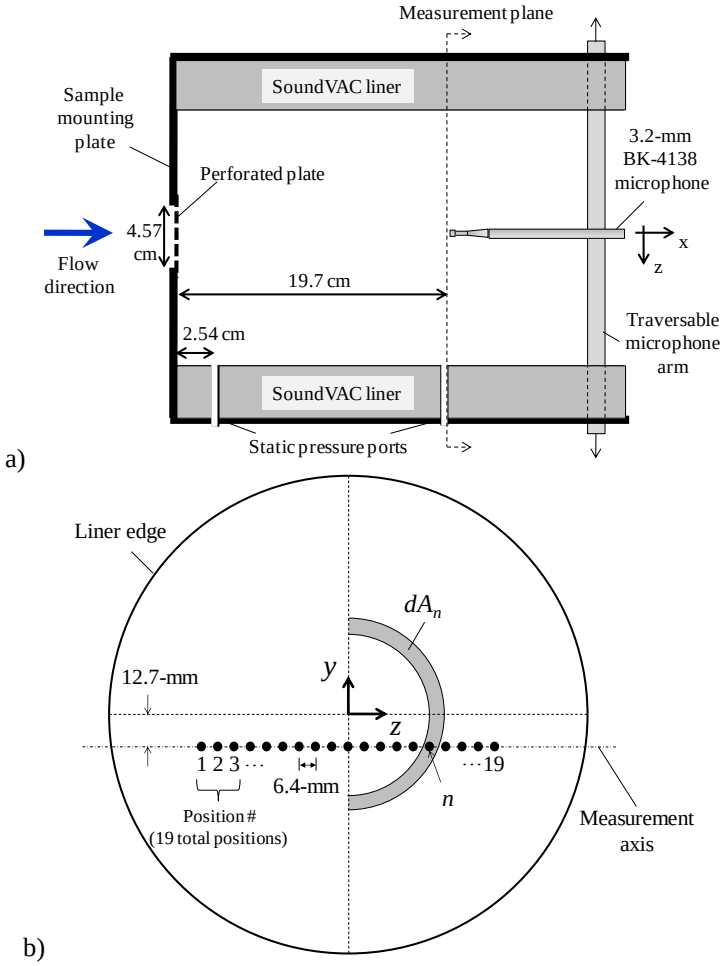

Fig. 5 Schematic detailing acoustic measurement of insertion loss, showing a) microphone position relative to the perforated; b) spatial locations in the measurement plane at which acoustic signals were acquired.

The acoustic intensity level spectrum was determined at 19 spatial location indicated by the dark circles, each separated by 6.4-mm. The acoustic intensity level for a plane wave in a non-stationary medium is related to the sound pressure

$$\mathrm{IL}_n = 10\log_{10}\left[(1+M_n)^2\,\frac{p_n'^2}{\rho c I_{ref}}\right] \tag{32}$$

n is the index corresponds to the measurement position in Fig. 5b, M_n is the Mach number, and $I_{ref} = 10^{-12}$ W·m^{-2} is the reference intensity. The intensity was assumed to be constant over the strip of area, dA_n, where the radii used to determine dA_n was selected to intersect the midpoint between the n and n-1, and the n and n+1 location along the measurement axis. M_n was determined from Pitot pressure measurements of the flow field downstream of the perforated plate and wall static pressure measurements on the measurement plane (Fig. 5a). In the current experiments, the Mach number on the measurement plane did not exceed 0.2 for all plates. Therefore the variation in density and temperature from a stationary medium did not exceed 2% and 1%, respectively, and the approximation $p^2_{ref} = \rho c I_{ref}$ holds satisfactorily, where $p_{ref} = 20\ \mu$Pa. This allowed the acoustic intensity level spectrum to be recast in terms of SPL

$$\mathrm{IL}_n(f) = 10\log_{10}\left[(1+M_n)^2\cdot 10^{0.1\cdot \mathrm{SPL}_n(f)}\right] \tag{33}$$

The sound power level is determined assuming the local intensity level spectrum is constant over the respective area dA_n

$$\mathrm{PL}_{\exp} = \sum_{n=1}^{19} \mathrm{IL}_n(f)\, dA_n \tag{34}$$

Figure 5b indicates that the sound power was determined based on a total area of 119.4-cm^2. Although the effective duct area is 275.5-cm^2, it will be shown in the results (Section IV) that this approximation of sound power was sufficient in obtaining trends which characterize the insertion loss of perforated plates our analysis. The expression for the experimentally determined insertion loss is

$$L_{I,\exp} = \mathrm{PL}_{0,\exp} - \mathrm{PL}_{\exp} \tag{35}$$

A total of 12 experimental cases were run: the baseline case (denoted with "0" subscript) where no perforation is installed, and 11 different perforated plates. The key parameters of each perforated plate used in the experiments are summarized in Table 2. In the experiments, the insertion loss was determined over a range of $0 \le M_1 \le 0.1$ for all plates.

Table 2 Properties of perforated sheets used in experiments.

Experiment	Porosity β	Thickness l, mm	Hole Diameter d, mm	Hole spacing P, mm	Perforation Grating
0	1.00	--	--	--	--
1	0.37	0.6096	1.1430	1.676	Square
2	0.48	0.4064	2.6162	3.353	Square
3	0.37	0.4064	1.1430	1.676	Square
4	0.29	0.4064	1.0160	1.676	Square
5	0.45	0.7620	1.7526	2.794	Triangular
6	0.23	0.7620	1.5875	3.175	Triangular
7	0.23	0.9144	1.5875	3.175	Triangular
8	0.23	0.4064	0.6858	1.270	Square
9	0.23	0.4064	0.6096	1.118	Square
10	0.22	0.4064	0.5080	1.016	Triangular
11	0.22	0.4064	0.4064	0.889	Triangular

IV. Results

A. Robustness of setup

An in-duct method was used to determine the total power of the acoustic wave at the measurement plane of the duct. In addition to sound pressure fluctuations from the source, the microphone is subject to additional unsteady turbulent pressure fluctuations associated with the flow itself[23]. The proposed model in Section II.B does not include unsteady pressure fluctuations from the mean flow. The frequency content of the microphone signal contaminated by pressure fluctuations associated with the flow was therefore identified before comparing with the theoretical prediction (Eq. 31). This was accomplished in two steps: examination of the signal-to-noise ratio between the acoustic signal and flow noise; and cross-correlations of the microphone signals acquired in the measurement plane.

The signal-to-noise ratio (SNR) was determined by comparing the sound power level spectra between two run conditions. For the first run condition, both the impinging jets source and mean flow were in operation. For the second run condition, only the mean flow was in operation, therefore isolating the spectral content associated with flow noise. The results are plotted in Fig. 6.

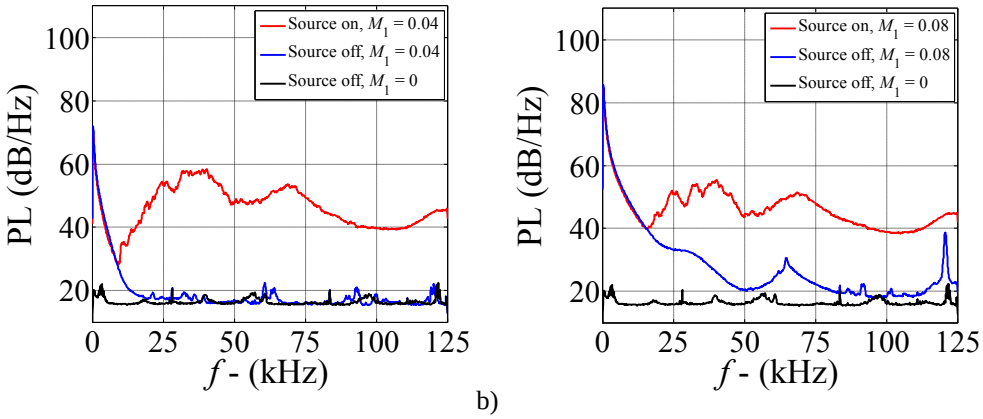

a) b)

Fig. 6 Sound power level spectra of flow conditions corresponding to both source and mean flow in operation (red line), only mean flow in operation (blue line), and background noise (black line) for Plate 1 at a) $M_1 = 0.04$; b) $M_1 = 0.08$.

The SNR is defined as the ratio of the acquired signal power to the unwanted noise power

$$\mathrm{SNR}_{\mathrm{dB}} = 10\log_{10}\left(\frac{p'^2_{signal}}{p'^2_{noise}}\right) \tag{36}$$

The signal power corresponds to the first run condition (both mean flow and impinging jets source on), and the noise power is associated with the second run condition (only mean flow on). Figure 6 indicates that the spectral content of flow noise is predominantly low-frequency, however at larger bias flow speeds (Fig. 6b), the flow noise also contains high frequency content. The extent to which low frequencies are contaminated by flow noise increases as the bias flow Mach number increases. At higher frequencies, there is a clear distinction in the power level spectrum between the two run conditions. Existing literature on in-duct acoustic measurements[23,24] recommended a minimum SNR of 10 dB to ensure accurate data recovery of an acquired signal. Therefore, only frequency components of the sound power level spectrum where the SNR $\geq$ 10 dB were considered valid in determining the insertion loss experimentally.

Microphone correlation data provided additional guidance in determining the amount of signal contamination due to turbulence fluctuations from the bias flow. The microphones tips were positioned approximately 19.7-cm downstream of the perforated plate (Fig. 7a). The microphones were fixed at positions 4 and 16 (Fig. 5b), which corresponded to a separation distance of 7.6-cm between the microphone tips. The microphone correlation results are plotted in Figs. 7b and 7c. The influence of bias flow on the cross-correlation is plotted in Fig. 7b for Plate 1. The signal correlation decreases with increasing Mach number, indicating an increasing dominance of flow noise over the acoustic signal from the impinging jets source. This trend of decreasing cross correlation with increasing bias flow speed was also observed for the remaining plates. There is a discernable peak near zero time lag for the static condition ($M_1 = 0$), however, the magnitude of the peak is significantly reduced as the bias flow Mach number is increased to $M_1 = 0.04$. In the range of $M_1 > 0.08$, no peaks are shown in the correlation plots, which indicate that the acoustic pressure field is largely contaminated by turbulence fluctuations associated with the bias flow. It is also noted that the time lag associated with the peak correlation does not shift appreciably with increasing bias flow, indicating a weak influence of wave front diffraction due to the mean flow.

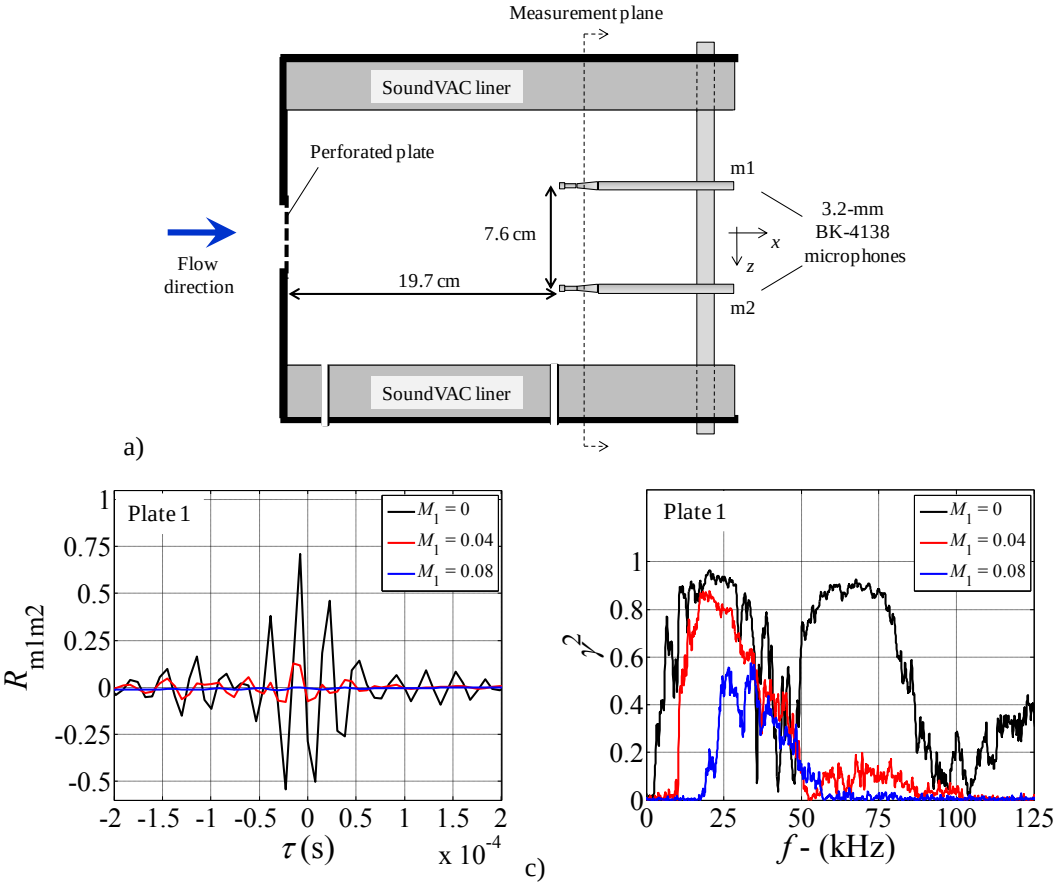

Fig. 7 Schematic of measurement setup for microphone correlation a) showing microphone positions inside measurement section; Correlation results for Plate 1, indicating the effect of increasing M_1 on b) cross correlation between microphone signals and; c) microphone coherence.

The coherence between the microphone signals was used to indicate frequencies at which signal contamination due to flow noise was most prominent. Figure 7c plots the dependence of coherence on the upstream Mach number. With increasing bias flow, the magnitude of coherence squared γ^2 decreases initially at high frequencies. Also, the limit at which low frequencies are incoherent broadens with increasing M_1. For all plates, the signal coherence rises from about 3 kHz at $M_1 = 0$, to about 22 kHz at $M_1 = 0.1$. To ensure that the incoherent frequency components of noise associated with flow were not factored into the insertion loss comparisons, a criterion of $\gamma^2 \geq 0.05$ was imposed in addition to the SNR criterion defined previously in this section.

B. Insertion loss

The comparisons between experimental measurements and theoretical predictions (Eq. 31) for insertion loss are shown in Figs. 8-11. Plates 1, 2, 6, and 11 were selected as representative cases that cover the range of porosity, hole diameter, and plate thickness used in the experiment. The insertion loss is plotted versus d/λ to facilitate the explanation of discrepancies between Eq. 31 and experiment. The insertion loss prediction and experimental measurements are in good agreement for $M_1 = 0$ (Figs. 8a-11a), which indicates that the proposed model is capable of accurately predicting insertion loss in the absence of bias flow. An exception is Plate 2 (Fig. 9a), where large discrepancies are observed for $d/\lambda > 0.6$. This is expected, due to higher order modes of acoustic propagation[21] that occur for $d/\lambda > 0.586$. As d/λ increases, Figs. 8 and 10 indicate a saturation followed by decline of insertion loss, while Figs. 9 and 11 indicate that the insertion loss increases monotonically. The difference in these two trends is attributed to standing-wave-formed resonances inside the contraction as the acoustic wavelength approaches the order of the plate thickness l. The resonance observed in the model predictions and experiment measurements are analogous to Fabry-Pérot-type resonance observed in optics[25]. The maximum resolvable frequency in our experiments corresponds to an acoustic wavelength that exceeds resonant conditions for thin plates (Figs. 9 and 11). As a result, peak insertion losses are confirmed experimentally only for thick plates (Figs. 8 and 10). Figures 8b,

10a, and 10b indicate that Eq. 31 is capable of predicting the frequency corresponding to peak insertion loss measured in the experiments.

Observing the behavior of Eq. 31 in Figs. 8-11, increasing the bias flow speed (M_1) results in two distinct trends: an increase in L_I at small values of d/λ, and decrease in the d/λ corresponding to peak L_I. The latter observation is a convection effect on the acoustic wave propagation by the mean flow in the contraction. The experimental measurements confirm these trends for Figs. 8-11 with good agreement except for Plate 6 (Figs. 10c and 10d), where the insertion loss decreases abruptly for $d/\lambda < 0.1$. Plate 11 also indicates a decrease in L_I as M_1 increases from 0.08 to 0.1. The departure between experimental measurements and Eq. 31 for Plates 6 and 11 is attributed to flow generated noise that was not removed based on the SNR and γ^2 criteria defined in Section IV.A.

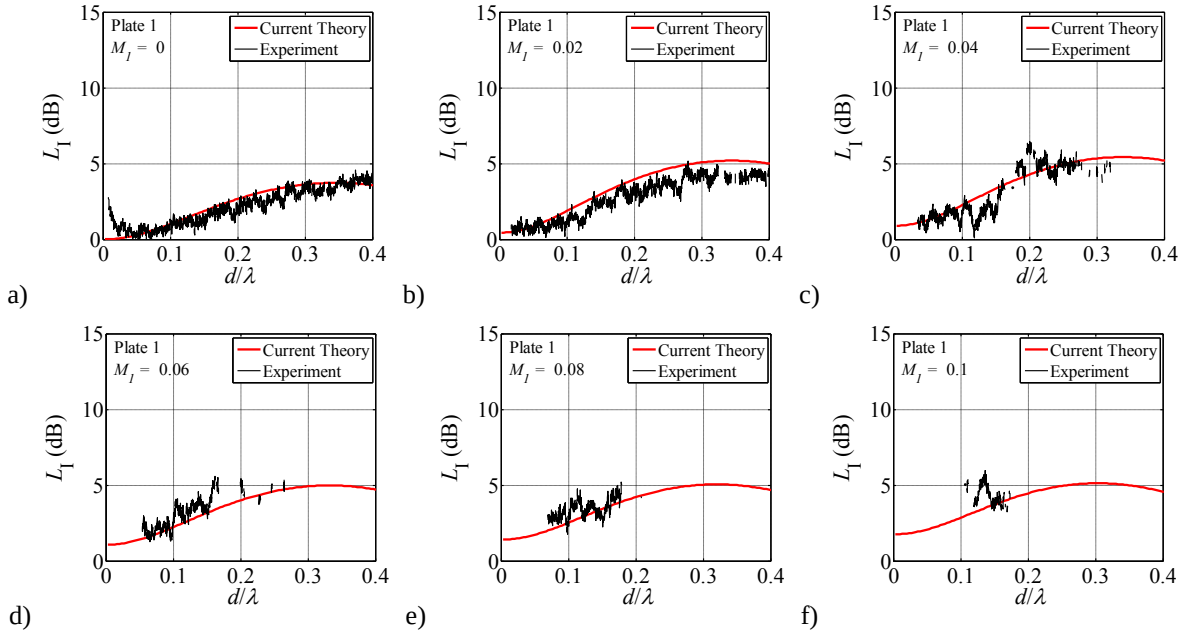

Fig. 8 Comparison between insertion loss predicted with Eq. 31 and experimental measurement for Plate 1. a) M_1 = 0; b) M_1 = 0.02; c) M_1 = 0.04; d) M_1 = 0.06; e) M_1 = 0.08; f) M_1 = 0.1.

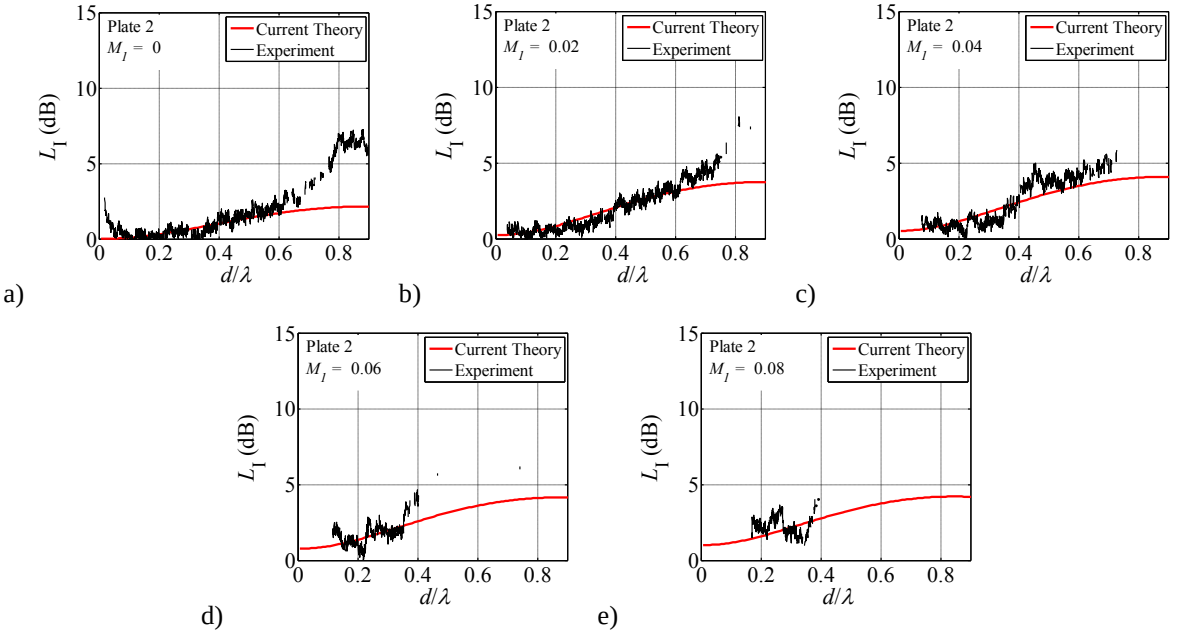

Fig. 9 Comparison between insertion loss predicted with Eq. 31 and experimental measurement for Plate 2. a) M_1 = 0; b) M_1 = 0.02; c) M_1 = 0.04; d) M_1 = 0.06; e) M_1 = 0.08.

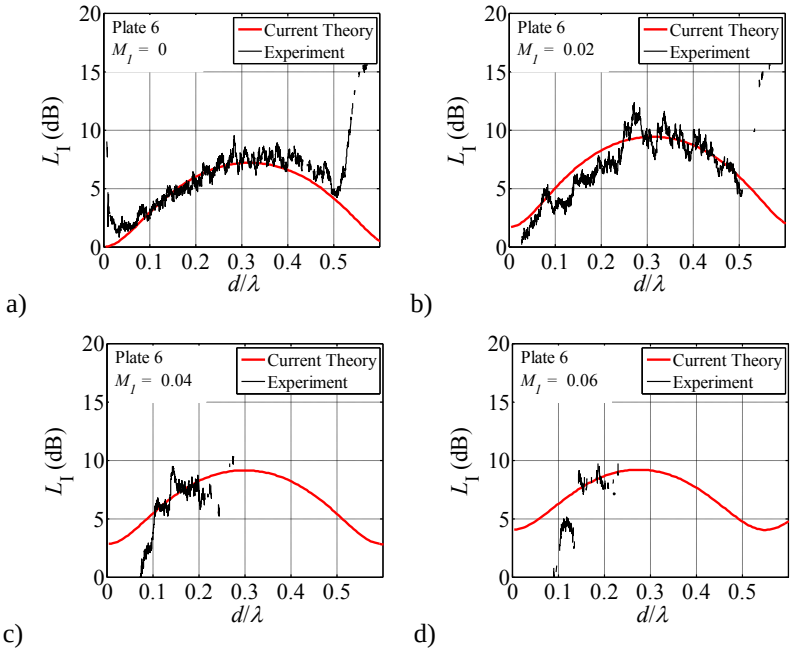

Fig. 10 Comparison between insertion loss predicted with Eq. 31 and experimental measurement for Plate 6. a) $M_1 = 0$; b) $M_1 = 0.02$; c) $M_1 = 0.04$; d) $M_1 = 0.06$.

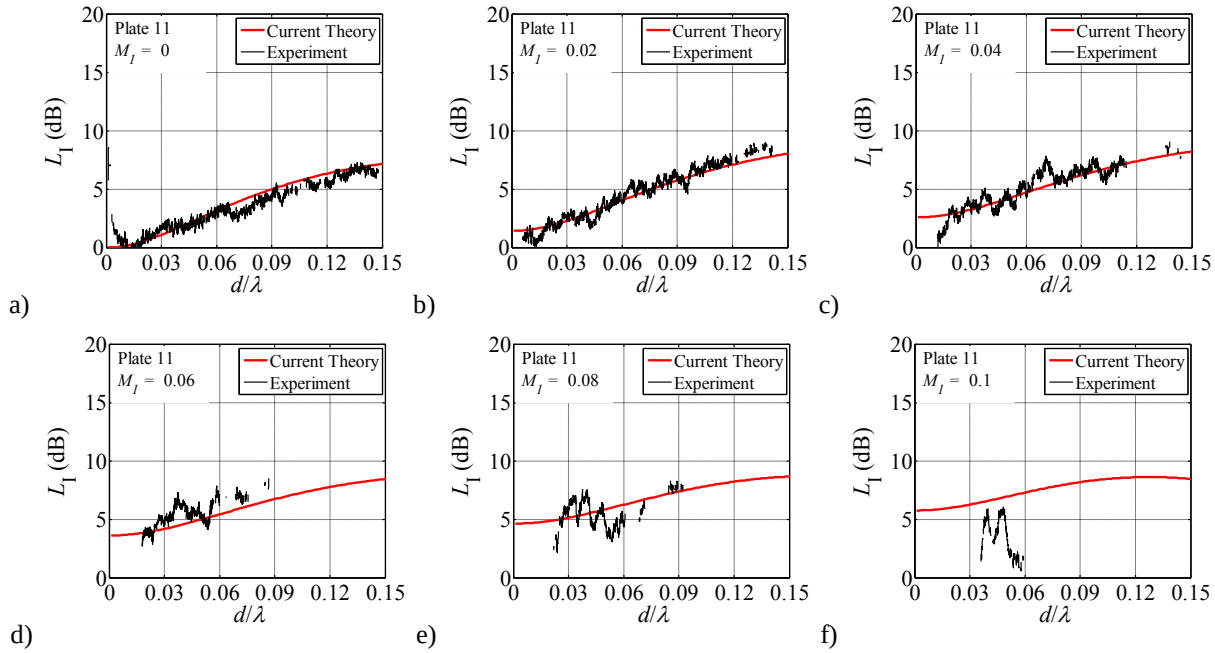

Fig. 11 Comparison between insertion loss predicted with Eq. 31 and experimental measurement for Plate 11. a) $M_1 = 0$; b) $M_1 = 0.02$; c) $M_1 = 0.04$; d) $M_1 = 0.06$; e) $M_1 = 0.08$; f) $M_1 = 0.1$.

The performance of Eq. 31 was next validated by comparison with the models of previous investigators[10,13,14]. Table 1 summarizes the range of bias flow Mach number, porosity, and dimensionless frequency d/λ over which previous theoretical models were validated. When comparing the proposed insertion loss model to previous models[10,13,14], a parameter space was selected to appropriately evaluate the current model. For comparison with previous models, the parameter range selected was $0.001 \leq d/\lambda \leq 0.02$, and $0 \leq M_2 \leq 0.35$.

Figures 12-15 compare the insertion loss predictions of the proposed model (Eq. 31), previous models[10,13,14], and the experimental measurements from this study. The vertical dashed line is drawn at $d/\lambda = 0.02$ for Figs. 12 and

13 to indicate the maximum d/λ validated for previous bias flow models. Within the range of validated d/λ, Eq. 31 yields more accurate predictions of insertion loss over previous models. Figures 12-15 indicate that all models predict an increase in L_1 with increasing bias flow. As described in Section I, the physical significance of this result is explained by the energy of the acoustic wave being transferred to the kinetic energy of vortical motions in the mixing region downstream of the perforated plate.

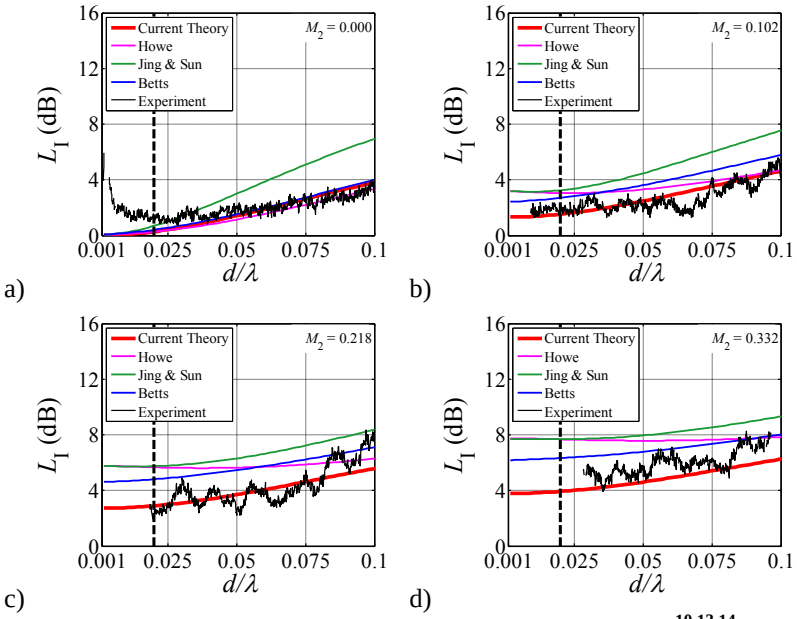

Fig. 12 Comparison between experimental measurement, previous models[10,13,14], and Eq. 31 for Plate 9 (β = 0.23, d = 0.61-mm, l = 0.41-mm). a) M_2 = 0; b) M_2 = 0.102; c) M_2 = 0.218; d) M_2 = 0.332.

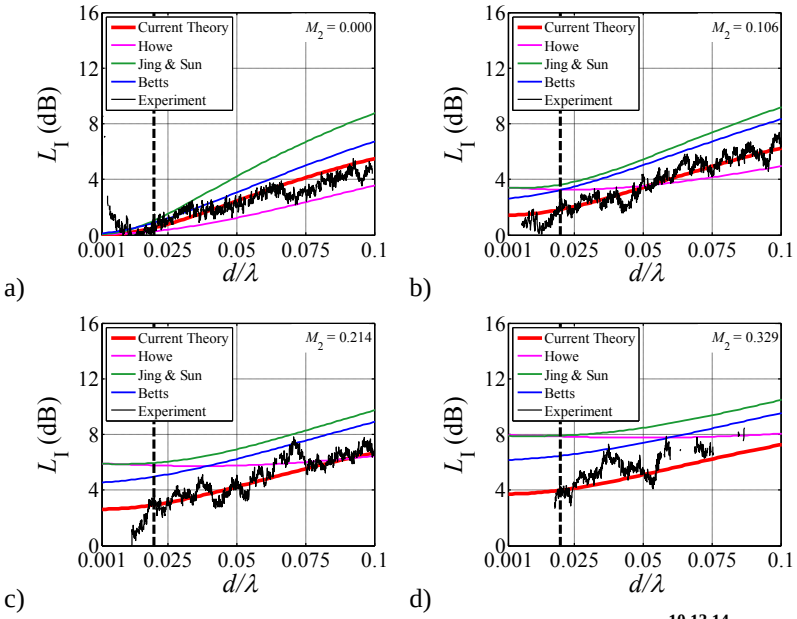

Fig. 13 Comparison between experimental measurement, previous models[10,13,14], and Eq. 31 for Plate 11 (β = 0.22, d = 0.41-mm, l = 0.41-mm). a) M_2 = 0; b) M_2 = 0.102; c) M_2 = 0.218; d) M_2 = 0.332.

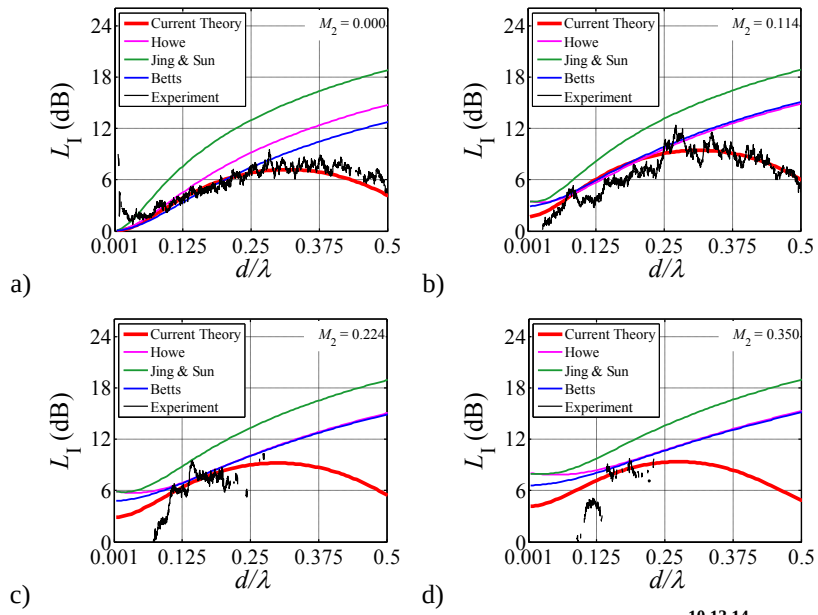

Fig. 14 Comparison between experimental measurement, previous models[10,13,14], and Eq. 31 for Plate 6 (β = 0.23, d = 1.59-mm, l = 0.76-mm). a) M_2 = 0; b) M_2 = 0.114; c) M_2 = 0.224; d) M_2 = 0.35.

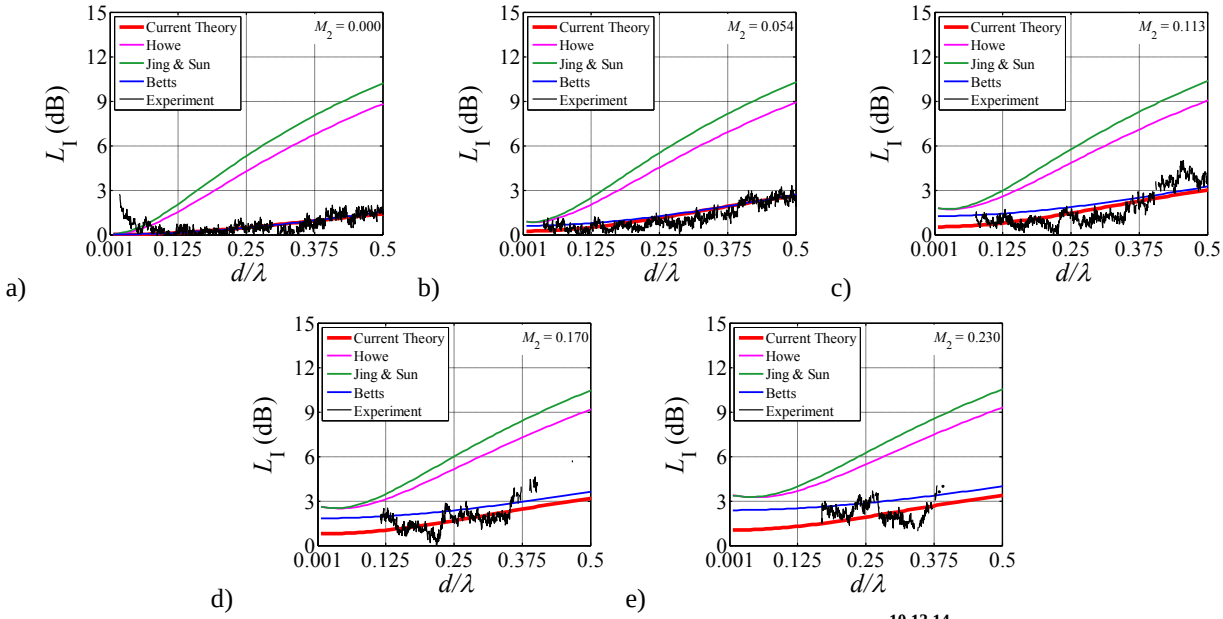

Fig. 15 Comparison between experimental measurement, previous models[10,13,14], and Eq. 31 for Plate 2 (β = 0.48, d = 2.62-mm, l = 0.41-mm). a) M_2 = 0; b) M_2 = 0.054; c) M_2 = 0.113; d) M_2 = 0.17; e) M_2 = 0.23.

The performance of the current (Eq. 31) and previous[10,13,14] bias flow models for $d/\lambda > 0.03$ was then evaluated against experimental measurements. For $M_1 = 0$, the insertion loss predictions using Howe's model[10] agrees with the current experimental data for small porosity perforates (Figs. 12 and 13). As porosity increases, Howe's assumption of no interaction between the perforations is no longer valid, and therefore his model becomes inaccurate for large β. This explains the large discrepancy between Howe's model and the experimental measurements shown in Fig. 15, where $\beta = 0.48$. Howe's model predicts a monotonic increase in insertion loss as the bias flow speed increases, which is consistent with the current experimental data for $0 \leq M_2 \leq 0.35$. His model, however, over-estimates the insertion loss increase at small d/λ (Figs 12b, 13b, 14b, and 15b).

Jing and Sun[13] modified Howe's model[10] with an impedance correction to include the effect of plate thickness. Jing and Sun's results show an increase in insertion loss in comparison to Howe's model at higher d/λ (Figs. 12-15). Since their model[13] is an extension of Howe's analysis, Jing and Sun's model also predicts additional low frequency attenuation when bias flow is present. Figures 12-15 indicate that the agreement between Jing and Sun's model and the current experimental data is very poor. The authors had noted in their work[13] that the additional reactance term corresponding to the thickness correction in their model resulted in an overestimate of the reactance when compared to their experiments. They claimed that reactance error was large at high bias flow speeds due to the effect of flow separation on the reactance, which was not included in their model.

Betts' impedance model[14] yielded similar trends as the models of Howe[10] and Jing and Sun[13]: an increase in insertion loss over the entire range of d/λ with increasing bias flow Mach number. The trends in his model are consistent with the current experimental results, however, his model slightly over predicts the insertion loss for many cases with low bias flow Mach number (Figs. 12b, 13b, and 14b). His model is very accurate for Plate 2 (Fig. 15), which is the highest porosity plate in this experiment. The large porosity implies a strong interaction between perforations, which Betts included in his model using Fok's function[18]. The importance of including hole interaction effects in the modeling of perforated plates with bias flow is emphasized by the greater accuracy in which Betts' model[14] and the proposed model (Eq. 31) predicts the insertion loss measurements for higher porosity plates, such as Plate 2.

Figures 14a and 14b indicate that all preceding models[10,13,14] do not resolve the saturation and decline in L_I that is characteristic of standing-wave resonance in the perforations. Also, the accuracy of all previous models are limited within the range of small d/λ, and small M_2 (Figs. 13a and 14a). The error between Howe[10] and Jing and Sun's[13] theory can be attributed to the low porosity approximations made in their work, and therefore the neglect of interaction effects. Although Bett's[14] model includes end effects, it fails to predict the low frequency increase in L_I accurately, with the exception of Plate 2. Observing that the proposed model (Eq. 31) predicts insertion loss with superior accuracy over previous models and is able to resolve the resonance phenomena for thick plates underpins the advantage of the current insertion loss model over previous models.

C. Accuracy of Proposed Model

To assess the range of validity of the current predictive model, Eq. 31, the deviation of the prediction from the experiment was examined systematically. The insertion loss error is defined as

$$\Delta L_I = L_{I,\text{model}} - L_{I,\text{exp}} \tag{37}$$

Equation 37 was used to determine the insertion loss difference between the proposed model Eq. 31 and experiments as a function of d/λ for Plates 1, 2, 6, and 11 (Fig. 16). Figure 16 indicates that ΔL_I stays within 2.5 dB for $d/\lambda < 0.4$ and $0 < M_1 < 0.02$. The discrepancy between the current model and experiment for Plate 2 at $d/\lambda > 0.7$ (Fig. 16b) and $M_1 = 0$ is due to higher order mode propagation as d/λ becomes larger than the cut-off frequency for plane waves. ΔL_I increases beyond 2.5 dB for Plate 6 (Fig. 16c) as M_1 increases to 0.06, while the remaining plates stay within 2.5 dB level difference. Plates 6 and 11 (Figs. 16c and 16d) indicate a large positive increase in ΔL_I as M_1 increases. From Eq. 37, this indicates that the insertion loss measured in experiments decreases with increasing bias flow for these plates, a trend that is not predicted from Eq. 31. This is more clearly illustrated in Fig. 17, where insertion loss contour levels are plotted versus d/λ and M_2.

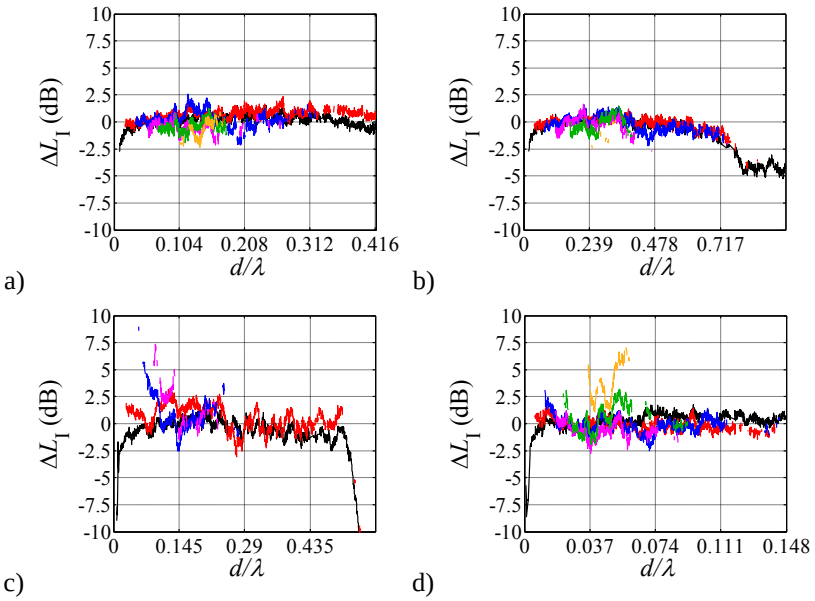

Fig. 16 Insertion loss error (Eq. 37) versus d/λ and M_1 for a) Plate 1; b) Plate 2; c) Plate 6; d) Plate 11

All subfigures of Fig. 17 indicate negative insertion loss, or noise amplification, at small d/λ. As the flow Mach number increases, the extent of d/λ which $L_I < 0$ also increases. This result is consistent with the signal-to-noise analysis in Section IV.A, where it was shown that the flow noise power spectrum progressively contaminates the low frequency content of the acquired signal as the mean flow speed increases. The white dashed lines in Fig. 17 indicate the Mach number where maximum insertion loss occurs for a specified d/λ. Plates 2 and 5 (Figs. 17a and 17b) do not provide conclusive information about peak L_I, however, Plates 9 and 11 indicate a nearly consistent trend of peak L_I at about $M_2 = 0.25$. As M_2 increases beyond 0.25, L_I decreases due to high frequency amplification from the flow (see Fig. 6b). The proposed model (Eq. 31) does not predict this behavior, and therefore the validity of the model is verified only for $M_2 < 0.25$. An explanation of why this trend was not observed for larger porosity plates (Figs. 17a and 17b) is that given the range of upstream Mach number tested in the experiment ($0 \le M_1 \le 0.1$), the maximum value of M_2 was not large enough to resolve any distinct trend of saturation and decline in L_I.

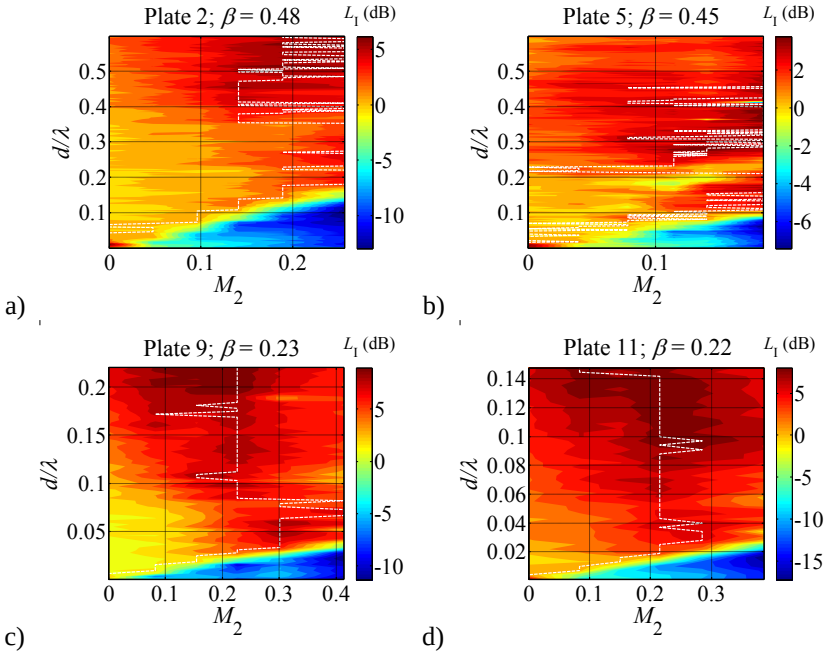

Fig. 17 Insertion loss contour plots versus error versus d/λ and M_2 for a) Plate 2; b) Plate 5; c) Plate 9; d) Plate 11. White dashed line indicates perforation Mach number of peak L_I for fixed d/λ.

Figure 18 plots ΔL_I with respect to l/d for Plates 1-11. The width of the error bars correspond to maximum and minimum ΔL_I between $0.02 < d/\lambda < 0.4$, and $M_2 < 0.25$ for a specific plate. The upper d/λ limit was selected to exclude large error magnitudes due to higher order modes (Fig. 16b and 16c). Figure 18 indicates a large amount of error localized between $0.45 < l/d < 0.6$. The large error can be explained by the assumption of a stable *vena contracta* downstream of the perforated plate. The location of the *vena contracta* was determined based on the jet profile by Rouse and Abul-Fetouh[20], and was assumed steady. Also, Rouse and Abul-Fetouh's analysis was based on a free jet issuing from a sharp edged orifice. The orifice thickness, which was not considered in their analysis[20], can have significant impact on the details of the jet profile. Smith[26] described multiple flow regimes for an orifice in a duct that depend on l/d. Smith identified a regime of thickness-to-orifice diameter ratio, $0.5 < l/d < 0.8$, where the jet may intermittently detach and reattach to the wall of the orifice. This transitional regime of separated or reattached flow implies unsteadiness of the *vena contracta*. Since both the insertion loss and end correction in this study are modeled based on steady flow, discrepancies between predictions and experiments could be attributed to the transitional regime of jet separation/reattachment described by Smith.

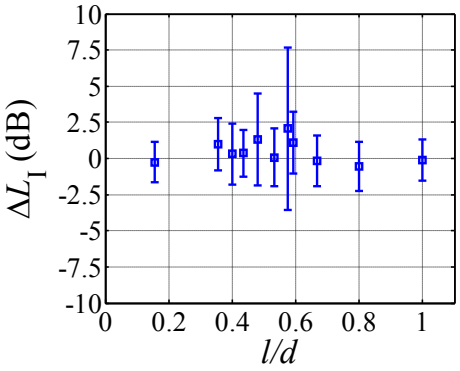

Fig. 18 Insertion loss error (Eq. 37) versus *l/d* for Plates 1-11.

The current analysis is valid only in quantifying the amount of transmitted energy from a known source upstream of the perforation. The experimental measurements (Fig. 17) indicated that noise regeneration as a result of turbulence fluctuations from the bias flow can significantly contaminate the fluctuations from the source, producing large errors between the proposed theory (Eq. 31) and experimental measurements. These effects were not included in the model, and therefore care was taken to isolate and omit any error arising from these sources of sound. The process of isolating these effects involved an examination of both signal-to-noise ratio and the microphone coherence in the measurement plane. The effectiveness of this method is critical in the validation of this study.

V. Conclusions

An experimental and theoretical parametric study of the acoustic damping characteristics of perforated plates at normal incidence with bias flow was conducted. The bias flow model developed in this study is based on one-dimensional wave propagation and mean flow through a single contraction/expansion chamber. The proposed model addresses certain aspects which previous models fail to investigate, namely the details of the bias flow *vena contracta* and the effect of the bias flow on end corrections of a perforated plate. The *vena contracta* of the jet that forms due to flow separation from the upstream corner of the contraction was modeled as an additional area reduction to the physical area contraction. The mean flow upstream of the contraction is approximately potential, and therefore the mass end correction upstream of the contraction was assumed equal to the end correction length used in classical studies without flow. The mean flow downstream of the *vena contracta* is no longer potential due to the mixing process between the jet and surrounding fluid. The end correction downstream of the contraction was therefore modified assuming that the attached mass downstream of the *vena contracta* location is destroyed. The bias flow mixing and viscous dissipation are sources of irreversible losses, which were included in the insertion loss model through entropy fluctuations.

The proposed model (Eq. 31) indicates a saturation and decline in insertion loss corresponding to standing-wave-formed resonance in the perforations as the acoustic wavelength approaches the thickness of the perforated plate. The dependence of resonant conditions on the plate thickness emphasizes the importance of accurately modeling the end correction of the perforated plate. Two primary trends were observed with increasing bias flow

Mach number: a monotonic increase in the insertion loss at low frequencies, and a decrease in the frequency corresponding to the peak value of insertion loss. The former observation is a result of flow losses due to mixing downstream of the area expansion. The latter observation is a convection effect on the acoustic wave propagation by mean flow within the contraction.

The experimental measurements obtained in this investigation confirm the trends observed in the proposed model for perforation Mach number $M_2 < 0.25$. At larger M_2, pressure fluctuations from the mean flow become significant such that a further increase in the bias flow Mach number results in a decrease in the sound attenuation capability of the perforated plate. This trend was only confirmed for low porosity plates; further experimental work at larger bias flow speed is needed to confirm this trend for plates with larger porosity. For $M_2 < 0.25$, and perforates outside the range of dimensionless thickness $0.5 < l/d < 0.8$, the proposed model agrees with experimental data to within 2.5 dB within the range of dimensionless frequencies $0.02 < d/\lambda \leq 0.4$. The proposed model yields superior insertion loss predictions than past models over the range of experiments in this study, and captures the resonance effect exhibited in thicker plates where previous models fail to do so.

References

1. Phong, V. and Papamoschou, D., "High Frequency Acoustic Transmission Loss of Perforated Plates at Normal Incidence," *Journal of the Acoustical Society of America*, Vol. 134, No. 2, 2013.
2. P. Mungur and G. M. L. Gladwell, "Acoustic wave propagation in a sheared fluid contained in a duct," *Journal of Sound and Vibration*. Vol. 9, No. 1, pp. 28-48, 1969D.
3. Ronneberger, "Experimental investigations of the acoustic reflection coefficient of discontinuous changes of cross section in tubes with air flow," *NASA TT F-14222*. 1972
4. R. J. Alfredson and P. O. A. L. Davies, "Performance of exhaust silencer components," *Journal of Sound and Vibration*. Vol. 15, No. 2, pp. 175-196, 1970
5. P. O. A. L. Davies, "Practical flow duct acoustics," *Journal of Sound and Vibration*. Vol. 124, No. 1, pp. 91-115, 1987
6. A. Cummings, "Sound transmission at sudden area expansions in circular ducts, with superimposed mean flow," *Journal of Sound and Vibration*. Vol. 38, No. 1, pp. 149-155, 1974.
7. G. C. G. Hofmans, R. J. J. Boot, P. P. J. M. Durrieu, Y. Auregan, and A. Hirschberg, "Aeroacoustic response of a slit-shaped diaphragm in a pipe at low Helmholtz numer, 1: Quasi-steady results," *Journal of Sound and Vibration*. Vol. 244, No. 1**,** pp. 35-56, 2001.
8. Durrieu, P., Hofmans, G., Ajello, G., Boot, R., Auregan, Y., Hirschberg, A. and Peters, M. C. A. M., "Quasisteady aero-acoustic response of orifices," *Journal of the Acoustical Society of America*, Vol. 110, No. 4, 2001.
9. Phong, V., Taghavi Nezhad, S., Liu, F., and Papamoschou, D., "Noise Reduction of a Turbofan Bleed Valve," *AIAA-2012-0681*, 50th Aerospace Sciences Meeting, Nashville, TN, Jan. 9-12, 2012.
10. M. S. Howe, "On the theory of unsteady high Reynolds number flow through a circular aperture," *Proceedings of the Royal Society of London*, Vol. 366, pp. 205-223, 1979.
11. I. J. Hughes and A. P. Dowling, "The absorption of sound by perforated linings," *Journal of Fluid Mechanics*, Vol. 218, pp. 299-335, 1990.
12. J. D. Eldredge and A. P. Dowling, "The absorption of axial acoustic waves by a perforated liner with bias flow," *Journal of Fluid Mechanics*, Vol. 485, pp. 307-335, 2003.
13. X. Jing and X. Sun, "Effect of plate thickness on impedance of perforated plates with bias flow," *AIAA Journal*, Vol. 38. No. 1. pp. 1573-1578, 2000.
14. J. F. Betts, *Experiments and Impedance Modeling of Liners Including the Effect of Bias Flow*, Ph.D. thesis. Virginia Polytechnic Institute, 2000.
15. I. B. Crandall, *Theory of Vibration System and Sound*, Van Nostrand, New York, 1926, pp. 229 et seq.
16. P. L. Smith and M. Van Winkle, "Discharge coefficients through perforated plates at Reynolds numbers of 400 to 3,000," *American Institute of Chemical Engineers Journal*, Vol. 4, No. 3, pp. 266-268, 1958.
17. I. E. Idelchik, *Handbook of Hydraulic Resistance 2nd Ed.*, Hemisphere Publishing Ca., 1986, Chap. 4, pp. 135-188.
18. V. A. Fok, "Teoreticheskoe issledovanie provodimosti kruglogo otverstiya v perogorodke, postavlennoi poperek truby (Theoretical study of the conductance of a circular hole, in a partition across a tube)," *Doklady Akademii Nauk SSSR*, Vol. 31, No. 9, pp. 875-878, 1941.
19. T. H. Melling, "The acoustic impedance of perforates at medium and high sound pressure levels," *Journal of Sound and Vibration*, Vol. 29, No. 1, pp. 1-65, 1973.

20. H. Rouse and A.-H. Abul-Fetouh, "Characteristics of irrotational flow through axially symmetric orifices," *Journal of Applied Mechanics*. Vol. 17, No. 50, pp. 421-426, 1950.
21. M. L. Munjal, *Acoustics of Ducts and Mufflers With Application to Exhaust and Ventilation System Design* John Wiley & Sons Inc., New York, 1987, Chap. 1, pp. 9-12.
22. Gerhold, C.H., and Clark, L.R., "Database of Inlet and Exhaust Noise Shielding for Wedge-Shaped Airframe," NASA/TM-2001-210840, April 2001.
23. W. Neise and F. Arnold, "On sound power determination in flow ducts," *Journal of Sound and Vibration*, Vol. 244, No. 3, pp. 481-503, 2001.
24. T. J. Mueller, C. S. Allen, W. K. Blake, R. P. Dougherty, D. Lynch, P. T. Soderman, and J. R. Underbrink. *Aeroacoustic Measurements*. Springer-Verlag Berlin Heidelberg. Ch. 1. pp 3-13, 2002.
25. B. Hou, J. Mei, M. Ke, W. Wen, Z. Lie, J. Shi, and P. Sheng, "Tuning Fabry-Pérot resonances via diffraction evanescent waves, *Physical Review B*, Vol. 76, No. 5, pp. 1-6, 2007.
26. A. J. W. Smith, *Pressure Losses in Ducted Flows*, Butterworth & Co., 1971, Chap. 4, pp. 135-188.